Rev. LatinAm. Metal. Mat.

Artículo Regular

www.rlmm.org

KINETIC CHARACTERIZATION OF AN AA8011 ALLOY NON-ISOTHERMALLY ANNEALED ABOVE 400ºC

Ney José Luiggi Agreda

Grupo de Física de Metales. Dpto. de Física. Escuela de Ciencias. Núcleo de Sucre. Universidad de Oriente. Cumaná. Venezuela.

Email. nluiggi@udo.edu.ve

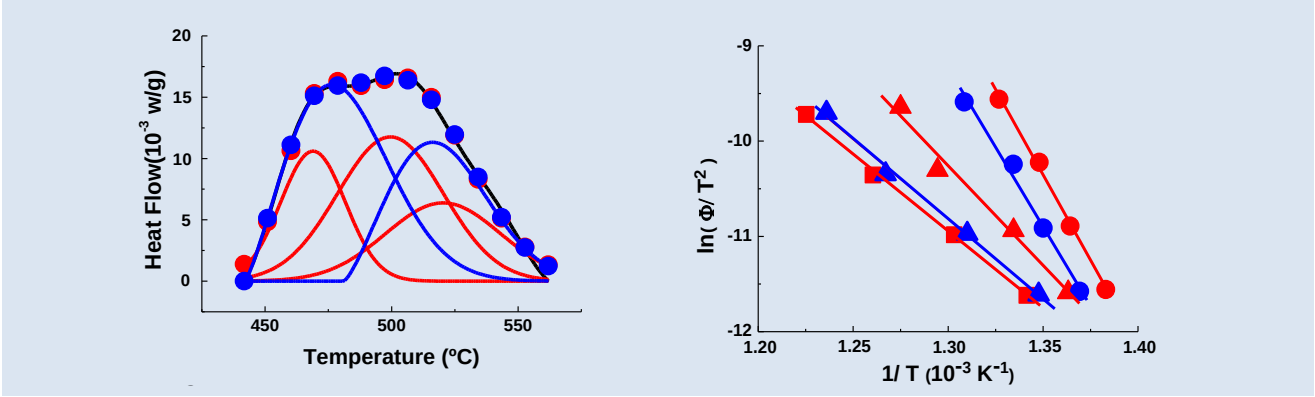

ABSTRACT

Solid state reactions occurring in an Al-Fe-Si alloy are demonstrated through DSC measurements at temperatures above that of recrystallization, where Fe-rich precipitation phases coexist with processes of recrystallized grain growth. These complex reactions are deconvolved for analysis into individual reactions associated to each of the transformation mechanisms involved in the process. Symmetrically distributed Gaussian transfer functions (GTF) and asymmetric Weibull transfer functions (WTF) are used in the deconvolution; and each individual reaction is analyzed through both the Šesták-Berggren (SB) combined kinetic model and the isoconversional scheme, a linear regression determining each of the parameters. The study reflects the drawbacks of kinetic analysis based solely on the fitting of heat flow, as the patent dispersion of kinetic parameters clearly shows. This is corrected by adjusting the activation energy obtained by isoconversion methods. Three reactions are required when using GTF; whereas only two suffice when using WTF. The overall results show that reactions above 400°C occur primarily because of Fe diffusion, and that other reactions occurring in deformed samples have activation energies coinciding with energy diffusion at high-angle grain boundaries.

Keywords: Kinetic Characterization, AA8011 Alloy, Reaction Rate Theory, Non-isothermal annealing.

CARACTERIZACIÓN CINÉTICA DE UNA ALEACIÓN AA8011 RECOCIDA NO-ISOTÉRMICAMENTE POR ENCIMA DE 400ºC

RESUMEN

A partir de medidas de DSC se pone en evidencia las reacciones que ocurren en una aleación Al-Fe-Si a temperaturas por encima de la temperatura de recristalización, donde coexisten los procesos de precipitación de fases ricas en Fe y el crecimiento de granos recristalizados. Para su análisis, estas reacciones complejas son deconvolucionadas en reacciones individuales asociadas a cada uno de los mecanismos de transformación involucrados en el proceso. En la deconvolución se utilizan funciones de transferencia simétrica de Gauss (GTF) y asimétrica de Weibull (WTF) y cada reacción individual se analiza a través del modelo cinético combinado de Sesták – Berggren (SB) y el esquema isoconversional; Y mediante regresión lineal se determinan cada uno de los parámetros involucrados. El estudio refleja las falencias del análisis cinético basado solo en el ajuste del flujo de calor, las cuales se manifiestan en una dispersión de valores de los parámetros cinéticos. Este hecho se corrige mediante la fijación de la energía de activación obtenida por el método de isoconversión. La data experimental es cubierta por tres reacciones cuando GTF son utilizadas, mientras que solo dos reacciones son suficientes cuando se usa WTF. Los resultados muestran en general que por encima de 400 ºC las reacciones ocurren principalmente por difusión de Fe y que en muestras deformadas ocurren otras reacciones cuya energía de activación coincide con la energía de difusión de contornos de grandes ángulos.

Palabras Claves: Caracterización Cinética, Aleación AA8011, Teoría de velocidad de reacción, recocido no-isotérmico.

Recibido: 22-04-2018 ; **Revisado:** 29-08-2018

Aceptado: 22-10-2018 ; **Publicado:** 10-01-2019

DOI: *10.5281/zenodo.7693764*

pISSN: 0255-6952 | eISSN: 2244-7113

Rev. LatinAm. Metal. Mat. 2019; **39** (1): 16-40

1. INTRODUCTION

The microstructural condition achieved by applying thermomechanical treatments on a material, conclusively regulates that material's properties. For example, the aim behind homogenization is, in principle, to create a matrix with few defects and submicroscopic atomic aggregates, so that subsequent annealing allows, with minimum perturbation, the identification of mechanisms generating any transformation in the material, as opposed to rolling, a process that introduces a large number of disturbances, mainly dislocations, in homogenized samples, that directly interact with any other processes, diffusive or otherwise, occurring in the samples. Under these premises it is expected that physical properties, susceptible to structural reordering of atoms and defects in the material, undergo modifications that can be simultaneously generated by more than a single physical mechanism. That is the case of the interaction between recrystallization and phase precipitation in deformed alloys, which is the subject matter of this work. The annealing process covers three major stages: recovery, recrystallization proper, and the growth of recrystallized grains. The first step in this crystal rearrangement is recovery, a process whereby deformed materials are annealed without the high-angle boundary migration [1] occurring below recrystallization temperatures. Both X-ray and electron microscopy have shown that dislocation density significantly decreases during recovery, dislocations tending to arrange themselves into sub-grain cell structures [2]. Haessner [3] has characterized the crystal changes occurring during recovery and recrystallization. Although the frontier between recovery and recrystallization is not well defined, it has been accepted that recrystallization starts with high-angle boundary migration [1]. However, the difference between recrystallization and grain growth lies in the source of the energy from which these processes derive. The energy required for recrystallization stems mainly from dislocation, whereas that for grain growth comes from grain boundaries [4,5], the latter also occurring at higher temperatures [5].

The third step identified in the annealing process is grain growth, which occurs at temperatures above that of recrystallization [5]. Although the recrystallization temperature is conceptually well defined, the fact is that different physicochemical factors affect its value, such as the microchemistry and composition of the material, the type and magnitude of the deformation [6], the temperature of annealing, the annealing time, and the thermal history of the sample (initial microstructure) [7,8].

This high incidence of the recrystallization process on the mechanical properties of alloys has led to an extensive literature for academic and industrial purposes, as on the one hand, academics and researchers need to understand how different mechanisms capable of magnifying the properties of the material occur and interact; and on the other, there is no end to the ever-expanding interest for lightweight, ductile and resistant materials with an optimal cost-investment ratio.

This effort has resulted in the implementation of thermo-mechanical treatments that enhance the refinement of the recrystallized grain [9,10], and are able to control or inhibit the formation of textures [7,11,12] that affect the formability of the material [13,14,15]. Furthermore, novel experimental techniques and theoretical studies have been incorporated [16-19] that lead to a better characterization of all the reactions taking place during annealing, which makes it possible to ascertain precisely when the restoration of the crystal has occurred. The softening of the deformed material after annealing, detected through yield stress variation, is revealed as one of the most effective methods to discern the evolution of recrystallization during annealing [7].

Furthermore, some authors have reported different behaviors during isothermal and non-isothermal annealing [20], basically because of the different ways in which both treatments modify the factors affecting each of the annealing stages. Sepehrban et al. [21] have studied the interaction of precipitation at each stage of non-isothermal annealing in an Al-Mg-Si-Cu alloy; and report different behaviors according to the heating rate. A similar effect is reported by Khani Moghanaki et al. [22] in a severely deformed 2024 aluminum alloy.

This work complements the experimental and theoretical studies carried out by the author and collaborators [23-25] on the effect of deformation on AA8011 alloys subjected to both isothermal and non-isothermal annealing. The use of DSC, thermoelectric power and its derivative highlights the existence of two transformations in the homogenized samples, one associated with precipitation of α-

AlFeSi at temperatures below 400°C, and another with β-Al3Fe near 470°C. Rolling accelerates the precipitation of the α phase up to a defined degree of deformation, suggestive of both reorganization of the dislocation structure and interaction between recrystallization and precipitation. Simultaneous interactions are established between precipitation of Guinier-Preston zones and other Si-rich aggregates and crystal recovery at temperatures below 150°C; and between α-AlFeSi phase precipitation and recrystallization in the 200 - 400°C temperature range.

Above 400ºC the β phase is less affected by the rolling process; and both DSC and the thermoelectric power derivative place the temperature at the start of β precipitation in the neighborhood of 400 ºC, coinciding with that at the final stage of recrystallization and growth of recrystallized grains. Pre-aging at different temperatures shows that recrystallization starts at 300°C. Transmission Electron Microscopy (TEM) shows the presence of recrystallized grains at both 475°C and 502°C. These results beg the conclusion that, above 400ºC, completion of recrystallization and grain growth in AA8011 alloys occurs simultaneously with Fe-rich phase precipitation.

Cordovilla et al. [26] by DSC, and Luiggi [27] by both DSC and thermoelectric power, report phase precipitation reactions above 400°C in AA8011, that undoubtedly involve Fe and Si diffusion. For both authors, recrystallization is strongly affected by the heating rate during non-isothermal annealing, this transfer occurring at a higher temperature when the heating rate is higher. These authors locate the recrystallization peak at 380ºC at heating rates of 40ºC/min [26], while Roy et al. [28] locate it at 352ºC for heating rates of 10ºC/min.

A diagram produced by Shoji et al. [29] reports both α-AlFeSi phase precipitation in a 70% cold-rolled AA1200 alloy occurring at temperatures of up to 400°C and the presence of Al_3Fe precipitates above that temperature. Raghavan [30], for his part, in his evaluation of the phase diagram of an Al-Fe-Si, identified up to seven compounds of different stoichiometry that may result as a consequence of the Fe/Si concentration ratio in the alloy; whereas Vybornov et al. [31] identified the presence of stable β-AlFeSi precipitates at 550°C. Other authors [32-34] have observed θ-Al_3Fe, α-AlFeSi, and β-AlFeSi phases reported as equilibrium phases. Kumar et al. [35] recently performed a deformation and recrystallization study on the microstructure and texture development of an AA8011 alloy, and found out that the annealing parameter combination to yield optimal texture deformation and recrystallization for improving this alloy's formability was 375ºC and 4 hours.

Luiggi [26] has confirmed that it is difficult to obtain pure reactions in multicomponent alloys, whereby a sole mechanism might account for the transformation measured. He also asserts that the kinetic analysis of the overall reaction is not always representative of the individual reactions that might occur. Hence, for a detailed analysis of the mechanisms involving the microstructural changes brought forth in the alloy, a mathematical procedure known as signal deconvolution [36-41] is used to separate the overall transformation in individual reactions. This paper endeavors, therefore, to determine the kinetic parameters associated to each individual transformation deconvolved from the overall reaction measured by DSC in AA8011 samples at temperatures above 400°C, where phase precipitation and grain growth process coexist.

The paper has been organized as follows: Section II introduces the theory of reaction kinetics and the isoconversion model, as well as the related deconvolution aspects. Section III elaborates on the experimental outlook; and Section IV parses the results and discussion.

2. THEORETICAL ASPECTS

2.1 On the kinetic theory

The theory necessary to carry out the present investigation totally corresponds with the one explained by Luiggi and Valera in this same journal [42], reason why the supporting equations have been obviated, and the reader is invited to review said reference.

We first consider the theory of reaction, where the reaction rate is defined by the time evolution of the extent of conversion α. Both the isothermal and the non-isothermal evolution of α follow the same equation, and the conversion from one to the other is achieved by introducing the heating ratio $\beta = dT / dt$. The reaction rate, in its simplest form, involves a reaction constant K (T), which in principle follows an Arrhenius relation (It is not always so [43]), and a kinetic function F (α) associated with the reaction's

generating mechanism. Similarly, this reaction rate can be determined directly from the measurements of heat flow duly weighed by the enthalpy of the reaction.

This approach relates the parameters defined in both K (T) and F(α) with the heat flow measurements obtained by DSC. The parameters of K (T) are the prefactor A and the activation energy Q, while the kinetic function selected is the truncated Šesták - Berggren [44,45], whose parameters are n and m. The kinetic analysis is, therefore, reduced to obtaining parameters A, Q, m, and n that reproduce the experimental data.

2.2 Evaluation of kinetic parameters

Considering the rate reaction equation, and explicitly including the expressions of K (T) and the Šesták-Berggren two-parameter kinetic function F(α) [44,45], the following equation is obtained (see appendix A),

$$\ln\left(\frac{\Delta H_{\alpha}}{S(1-\alpha)^{n}\ \alpha^{m}}\right) = \ln(A) - \frac{Q}{RT} \qquad (1)$$

where $\Delta H_{\alpha} = \int_0^{t_\alpha} \Delta H dt$ represents the area under the heat flow curve ΔH from the start of the reaction until a time tα has elapsed. The best m and n values linearizing Equation (1) were obtained by linear regression with an R2(L) determination factor closer to 1. The conversion extent α was limited to the range between 0.05 and 0.95, a range larger than that of our previous study [42], basically to take advantage of the best tail effect that Weibull functions grant to fittings of experimental data. At this stage it is worth wondering whether a relation of uniqueness exists between parameters n and m in Equation (1) and the value -Q/R guaranteeing that equation's linearity. The answer is negative since different sets of parameters might well adjust the experimental data in such a way that Equation (1) is a straight line; however, the ambiguity over parameters can be reduced by directly deriving the activation energy by isoconversion [25].

As for activation energy, there is such an implicit dependence of ΔH on β that its value is mainly regulated by the natural logarithm of the quotient between the experimental data and the kinetic function adjusted for these data. The literature shows that for processes involving crystallization, there exists a decreasing dependence on Q when β increases [46]; however, there seems to be no reference in the literature for processes involving the coexistence of several processes, making it impossible to obtain an activation energy independent from experimental data, sample geometry, and heating rate [47].

2.3 The Isoconversion Method

The isoconversion method is based on the fact that for the same conversion extent α, the functions depending on α will remain constant. For example in Equation (1) there will be a ΔH curve for each heating ratio β, and therefore, the function F(α) in the denominator of that relation will remain constant for a fixed value of α in each of the β considered. This implies that in order to have access to the activation energy, explicit knowledge of the kinetic function is not required in advance. In this work, the activation energy is evaluated using the isoconversion relation referenced in [48], the temperature peaks for different values of β being identified from the deconvolved curves,

$$\ln\left(\frac{\beta}{T^{N}}\right) = \ln(A) - \frac{Q}{RT} \qquad (2)$$

where T represents the peak temperature of the deconvolved reaction; and β, the respective heating rate. This relation allows for the graphic determination of Q and A values for a known value of N. The dispersion of the Q values inferred for the same microstructural condition and different β from the previous section does not allow a single reference value of Q to determine the best value of N and the other kinetic parameters. Hence, N=2, which is equivalent to using Kissinger's relation [49]. Resorting to other N values, in harmony with other models in the literature, generates Q values not very different from those obtained via the Kissinger method. Since isoconversion methods get their true meaning when the kinetic triplet is specified, to wit: Q, A, and F(α) [50], certain approximations are frequently used to finally assess the additional parameters appearing in the different kinetic functions; e.g., the N evaluation in the JMAEK scheme [51].

The methodology followed in this work purports to ascertain Q from Kissinger plots and then use Equation (1) to obtain, from Šesták-Berggren, n and

m values that linearize that equation in an energy range defined by Q ± 0.005 Q.

2.4 Deconvolution of experimental curves

The analysis of overall signals in multiple response systems tends to arrive at conclusions masking actual individual results. Such is the case of differential thermal analysis in multicomponent alloys where the signal measured covers a number of particular effects only separable by mathematical deconvolution techniques.

Deconvolution is a highly important tool in the treatment of signal processing based on the principle of linearity and time invariance of the signal. The convolution integral defines the output signal Y(t) generated by one or several input impulses X(t) owing to a transfer function g(t) [52,53]:

$$Y(t) = X(t) * g(t) = \int_{-\infty}^{\infty} X(\tau) g(t-\tau) d\tau \quad (3)$$

The opposite of convolution is deconvolution, whereby knowing the output Y(t) and the transfer function g(t), it is possible to determine the attainable input functions generating said output [54]. In this study, the output signal is the heat flow measured by DSC. The wide array of transfer functions available can determine particular input signals.

Deconvolution in this paper is performed by means of PeakFit (Systat Software Inc.), whose great versatility in signal separation and analysis, and its spectroscopy, chromatography, statistics and miscellaneous sections, allow for conclusive results of a wide variety of peaks. Two types of transfer functions were selected for this analysis.

1. Gaussian Function [55]:

$$W = W_0 \, exp\left[-\frac{1}{2}\left(\frac{T-W_1}{W_2}\right)^2\right] \quad (4)$$

where W represents heat flow; T, the temperature; and W_0, W_1, and W_2 represent the amplitude, center and width of the curve, respectively.

2. Weibull Function [56]:

$$W = W_0 \left(\frac{W_3-1}{W_3}\right)^{\frac{1-W_3}{W_3}} \left(\frac{T-W_1}{W_2} + \left(\frac{W_3-1}{W_3}\right)^{\frac{1}{W_3}}\right)^{W_3-1} \exp\left[-\left(\frac{T-W_1}{W_2} + \left(\frac{W_3-1}{W_3}\right)^{\frac{1}{W_3}}\right)^{W_3} + \frac{W_3-1}{W_3}\right] \quad (5)$$

which includes a fourth parameter, W_3, that regulates the form or asymmetry of the peak.

3. EXPERIMENTAL

3.1 Samples studied

An Al-Fe-Si alloy, commercially known as AA8011, was selected, supplied in as-cast form by C.V.G. ALCASA Venezuela, after a process of twin-rolling, cast in 6-mm strips, and then milled to 0.5 mm. It is from samples with this latter thickness that the homogenization and rolling treatments of the present study are initiated. Its composition is provided in Table 1.

Table 1. Chemical composition of alloy AA8011 (wt%).

Al	Fe	Si	Mn	Zn	Cr	Cu
Rem	0.56	0.40	0.01	0.004	0.003	0.01

3.2 DSC equipment and thermal treatment

Heat flow was measured with a Netsch STA-Jupiter 499 calorimeter, whose sensitivity allowed detection of very small heat flow fluctuations.

Three initial microstructural conditions were considered: 1. Samples homogenized during four hours at 600°C, then quenched in water at 2°C (HS); 2. HS samples cold rolled down to 50% gauge in a two-high rolling mill, hence the designation 50-DHS; and 3. Samples similar to those of condition No. 2 but having undergone an 85% thickness reduction, designated as 85-DHS.

To evidence the reactions occurring above 400°C, in particular Fe-rich phase precipitation and grain growth, samples were heated between room temperature and 600°C, the temperature range above 400ºC being selected for each of the samples considered.

4. RESULTS AND DISCUSSION

4.1 Heat flow measurements

Figure 1 displays heat flow variation versus temperature for the AA8011 alloy in HS samples heated at different rates.

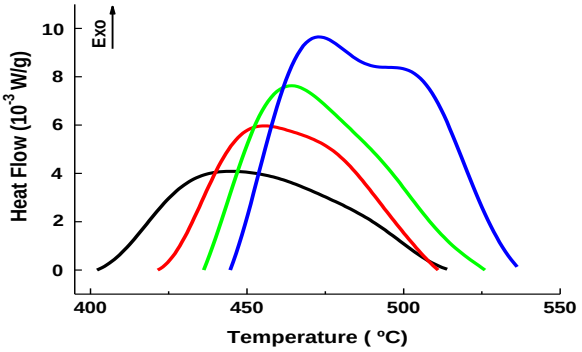

Figure 1. Heat flow versus temperature for HS samples of an AA8011 alloy at different heating rates (β). Black: 5ºCmin^{-1}. Red: 10ºCmin^{-1} Green: 20 ºCmin^{-1}. Blue: 40 ºCmin^{-1}.

The figure shows the complex diffusive-like reaction that seems to be a consequence of at least two physical mechanisms, evident at the 40°Cmin-1 curve. Fe-rich phase precipitation has been reported for this microstructural condition at that temperature range, especially that of Al3Fe and Al-Fe-Si of variable composition [30,31]. Heat flow, and particularly the peak of the reaction, increases as the heating rate increases, heralding larger enthalpy reactions.

Figure 2 shows the heat flow variation versus temperature for 50-DHS samples of an AA8011 alloy at different heating rates.

The behavior shown in this figure seems less complex than that of HS samples, although the difference in kinetics indicates the existence of one or several different reactions with respect to the previous one. The rolling effect seems to generate a microstructural rearrangement. In addition to the phases already indicated for the homogenized samples, high-angle boundary migration and the development of recrystallized grains are expected [4]. As in the previous case the reaction peak is higher for larger β. This result implies that a moderate rolling process favors the precipitation of phases once the recovery and recrystallization processes have taken place, since the tangle of defects and dislocations capable of anchoring the atomic movement has disappeared.

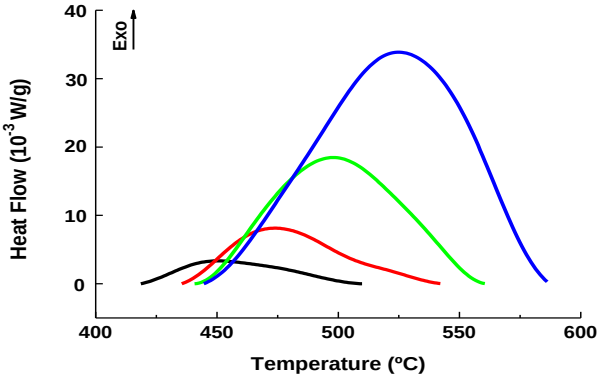

Figure 2. Heat flow versus temperature for 50-DHS samples of an AA8011 alloy at different heating rates (β). Black: 5ºCmin^{-1}. Red: 10ºCmin^{-1} Green: 20 ºCmin^{-1}. Blue: 40 ºCmin^{-1}.

Figure 3 plots heat flow versus temperature of an AA8011 alloy for 85-DHS samples heated at different heating rates. A complex behavior is reflected here, different from the prior one due to the larger number of defects and irregularities introduced in this type of sample.

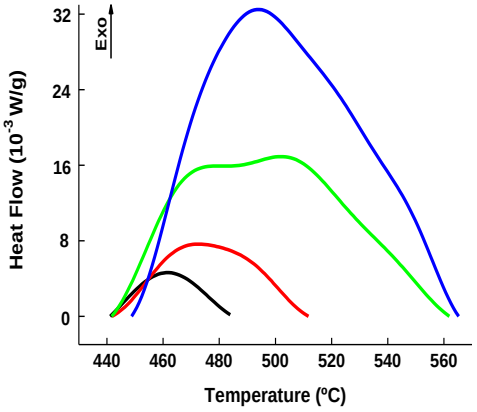

Figure 3. Heat flow versus temperature for 85-DHS samples of an AA8011 alloy at different heating rates (β). Black: 5ºCmin^{-1}. Red: 10ºCmin^{-1} Green: 20 ºCmin^{-1}. Blue: 40 ºCmin^{-1}.

4.2 Deconvolution of heat flow curves

Experimental kinetics are first deconvolved using Gaussian and Weibull transfer functions, both defined in Section 2.4. The validity criterion to fit theoretical and experimental data is set through the determination regression coefficient R2(D), a

minimum value of 0.99 being required for this adjustment to be considered valid. The number of reactions during deconvolution is set by this criterion. The kinetics deconvolution for the three microstructures under study required, in each case, three reactions when Gaussian transfer functions were used, and two when using Weibull. This difference in the number of reactions might cast doubts on the efficacy of the method to determine the mechanisms generating the kinetics; it is, however, a consequence of the symmetry of the Gaussian function and the asymmetry of Weibull functions.

4.2.1 Kinetic deconvolutions in HS samples

Figure 4 displays heat flow variation versus temperature, as a result of the experimental data's deconvolution measured at different heating rates in homogenized AA8011 samples using Gaussian transfer function.

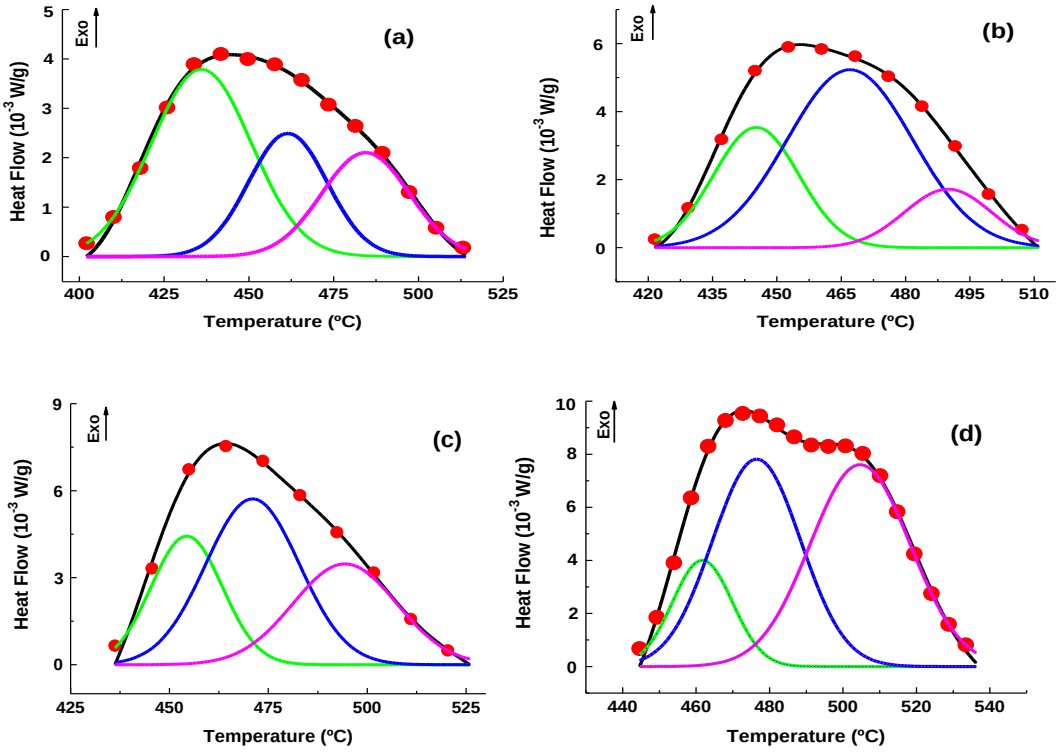

Figure 4. Deconvolution plots using Gaussian transfer function showing heat flow vs temperature for HS samples for different heating rates. a. 5 ºCmin^{-1} b. 10 ºCmin^{-1} c. 20 ºCmin^{-1} d. 40 ºCmin^{-1}.

Both the experimental and theoretical curves are highlighted in each of these figures, in addition to the different reactions obtained by deconvolution. In principle, for this microstructural condition, precipitates of differing Fe/Si ratios, and stable Al3Fe phase precipitates are expected to coexist. The possibility of co-existence of these reactions is enhanced by Langsrud [57], where intermetallics with different structures can be formed depending on the Fe/Si ratio in Al-Fe-Si alloys. Each deconvolved reaction can be characterized by both the position of its peak and its enthalpy, although there is no way to identify any of them, despite the fact that the first one in Figure 4.a; the second, in Figures 4.b and 4.c; and the third, in Figure 4.d, show areas larger than those of the others.

These reactions confirm that phase precipitation in multicomponent commercial alloys does not occur by means of a unique reaction, even though the DSC curves show a single peak.

The same experimental data are analyzed using Weibull transfer functions. This analysis is presented in Figure 5. Due to the asymmetry of this transfer function, only two reactions are needed to meet the condition R2 >0.99.

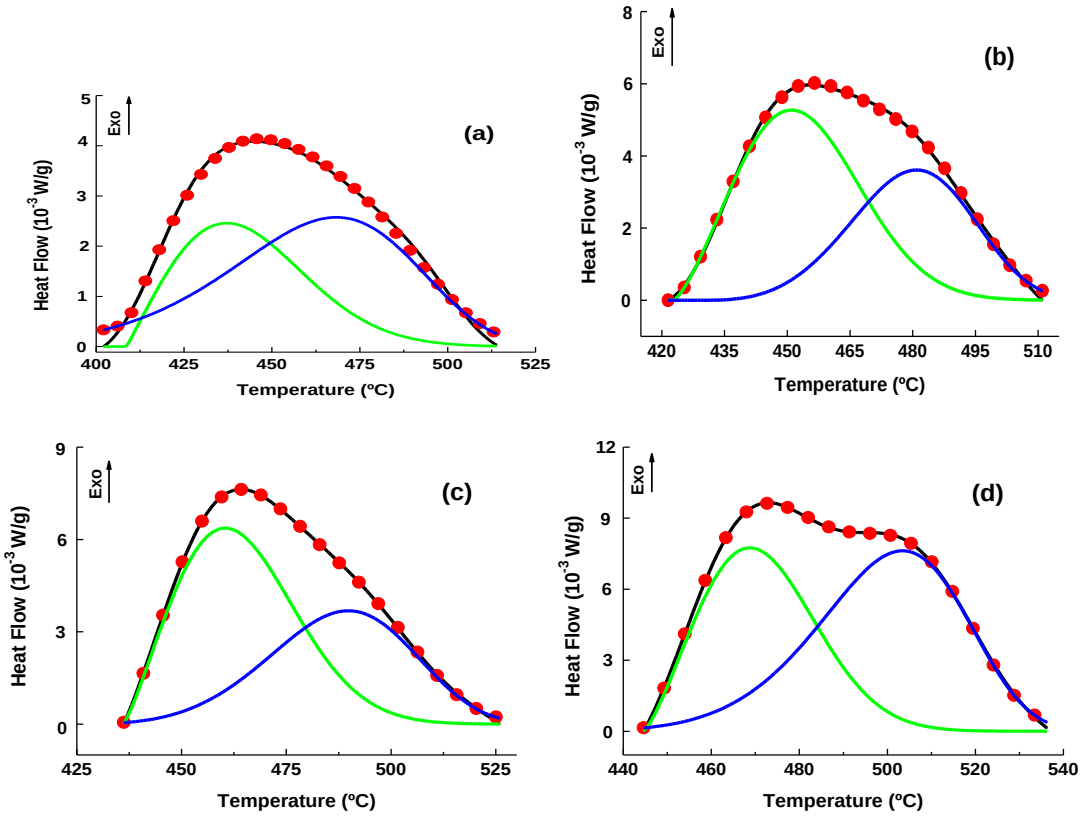

Figure 5. Deconvolution plots using Weibull transfer function, showing heat flow vs temperature for HS samples for different heating rates. a. 5 ºCmin^{-1} b. 10 ºCmin^{-1} c. 20 ºCmin^{-1} d. 40 ºCmin^{-1}.

Deconvolved reactions are not so different in area, a condition that poses competitiveness between the two precipitation mechanisms generating the experimental kinetic. The diffusive character of the mechanisms controlling the reactions and moving the peaks towards the high temperatures when the heating rate is greater is a confirmation of the coexistence of both reactions, as shown in particular by Figure 5.d.

Table 2 displays Wi deconvolution parameters for HS samples. It also includes the total transformation area (Stotal: Total area under the reaction curve) and the area for each particular reaction. Stotal increases as heating ratio β increases, the particular areas not following the same pattern. A similar disposition can be observed in W1, corresponding to the temperature of maximum transformation in °C, each reaction reaching higher temperatures as β increases, confirming that each of these particular reactions hinges on a diffusive mechanism. As for the value of R^2, a better overall reproduction of the experimental data can be attained when Weibull functions are used, owing to W3 reflecting in all cases the asymmetry of both reactions, and reproducing more effectively the start and endpoints of the experimental curve.

Table 2. Deconvolution parameters for Gaussian and Weibull transfer functions for AA8011 HS samples.

β °C min^{-1}	S_{Total}	R^2 TF	Reaction	W_0	W_1	W_2	W_3	S
5	0.28029	0.9968 G	1	0.0037906	436.000	14.713		0.1398
			2	0.0024932	461.486	11.562		0.0722
			3	0.0021034	484.419	12.941		0.0682
10	0.32388	0.9984 G	1	0.0035368	445.181	9.9228		0.0879
			2	0.0052311	467.027	14.6608		0.1922
			3	0.0017200	489.894	10.1282		0.0437
20	0.38410	0.9975 G	1	0.0044363	453.366	8.99940		0.1000
			2	0.0057198	471.009	11.8355		0.1698
			3	0.0034773	494.361	13.1239		0.1144
40	0.57662	0.9977 G	1	0.0040091	461.729	8.13644		0.0818
			2	0.0078178	576.483	12.0109		0.2354
			3	0.0076098	504.685	13.6032		0.2595
5	0.28512	0.9948 W	1	0.0024598	437.141	39.6436	2.0433	0.1121
			2	0.0025749	468.323	197.766	7.9333	0.1730
10	0.32214	0.9989 W	1	0.0052717	451.022	35.4609	2.4040	0.1909
			2	0.0036096	480.933	56.9331	4.0920	0.1312
20	0.38135	0.9998 W	1	0.2229891	460.422	32.0313	2.1964	0.2230
			2	0.1583588	489.789	74.324	4.5808	0.1584
40	0.57288	0.9997 W	1	0.2508606	468.758	30.8704	2.3229	0.2509
			2	0.3220156	503.422	104.750	6.6623	0.3220

4.2.2 Kinetic deconvolutions in 50-DHS samples

Figure 6 displays the kinetic deconvolutions in 50-DHS samples using Gauss transfer functions. Under this microstructural condition at that temperature range, the precipitation occurring in HS samples and a process associated to recrystallized grain boundary migration must ensue.

Furthermore, owing to different factors modifying recrystallization some remnants of this precipitation process should be considered. Although three Gaussian functions are needed for the experimental data reproduction, in each case one or two reactions would prevail, which can be associated to the precipitation process, whereas the remaining lesser-enthalpy reaction might be related to high-angle grain boundary migration or grain growth.

Figure 7 shows the kinetic deconvolution in 50-DHS samples using Weibull transfer functions. Two deconvolved reactions are shown. This behavior is the comportment expected for a homogenized, quenched, and 50% cold-rolled microstructure, where a strong reaction associated with the precipitation of an iron-rich phase is simultaneously manifested with a reaction of much lesser enthalpy associated to grain growth. Moderate rolling seems to have a double effect on kinetics, the first one generating an atomic arrangement with a propensity to favor only one kind of precipitates; and the second, inducing a simultaneous reaction associated to grain growth, the enthalpy in this second reaction augmenting as β increases. This result seems ideal to analyze the interaction between phase precipitation and recrystallized grain growth.

Table 3 shows deconvolution parameters obtained for kinetics in 50-DHS samples. The increase of Stotal

with a β increase is again reported, as well as the diffusive character of the individual reactions. Deformation, with respect to HS samples, increases the overall area under the transformation (except for 5°Cmin-1), a phenomenon suggestive of another mechanism or other mechanisms taking place for samples with this microstructural condition. The asymmetry of the precipitation reaction changes little with β increase; unlike that of the second reaction, which grows significantly as β increases.

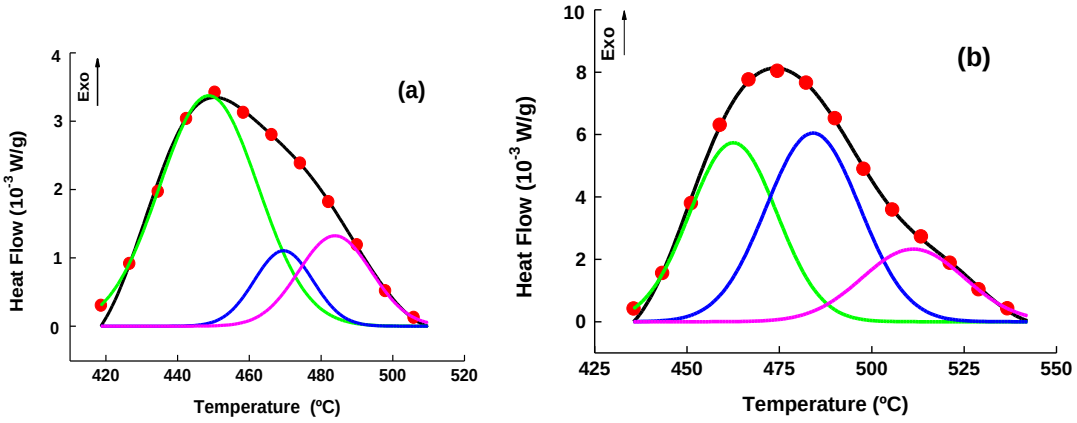

Figure 6. Deconvolution plots using Gaussian transfer function and showing heat flow vs temperature for 50-DHS samples for different heating rates. a. 5 ºCmin^{-1} b. 10 ºCmin^{-1} c. 20 ºCmin^{-1} d. 40 ºCmin^{-1}.

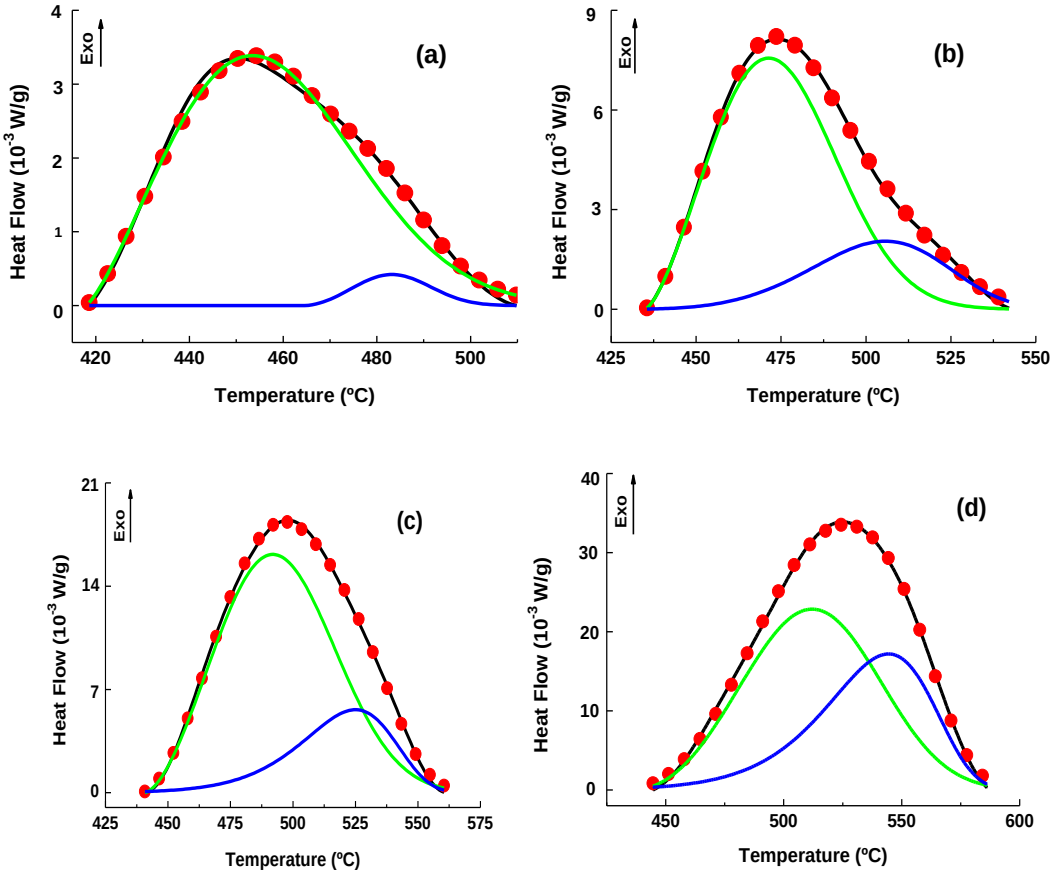

Figure 7. Deconvolution plots using Weibull transfer functions, showing heat flow vs temperature for 50-DHS samples for

different heating rates. a. 5 ºCmin^{-1} b. 10 ºCmin^{-1} c. 20 ºCmin^{-1} d. 40 ºCmin^{-1}.

Table 3. Deconvolution parameters for Gaussian and Weibull transfer functions for AA8011 50-DHS samples.

β ºC min^{-1}	S_{Total}	R^2 TF	Reaction	W_0	W_1	W_2	W_3	S
5	0.17251	0.9955 G	1	0.0033738	448.701	13.743		0.1162
			2	0.0011042	469.551	8.1679		0.0226
			3	0.0013243	483.889	10.144		0.0337
10	0.44299	0.9986 G	1	0.0057416	462.520	11.809		0.1699
			2	0.0060486	484.105	12.697		0.1925
			3	0.0023289	511.241	13.795		0.0805
20	1.20577	0.9990 G	1	0.0061853	471.227	12.276		0.1903
			2	0.0179419	499.744	18.718		0.8418
			3	0.0055669	531.297	12.442		0.1736
40	2.63450	0.9992 G	1	0.0097836	482.661	16.553		0.4059
			2	0.0321446	521.404	21.890		1.7638
			3	0.0127612	553.430	14.530		0.4648
5	0.17187	0.9952 W	1	0.0033864	453.446	45.6784	2.2950	0.1637
			2	0.0004303	483.315	21.9301	2.8486	0.0082
10	0.44083	0.9990 W	1	0.0075606	471.362	44.9460	2.4803	0.3386
			2	0.0020494	505.724	90.0385	4.7940	0.1022
20	1.20455	0.9990 W	1	0.0161558	491.938	61.3540	2.6655	0.9319
			2	0.0056271	525.019	311.876	17.468	0.2726
40	2.63627	0.9989 W	1	0.0228547	512.057	86.6841	3.1701	1.6063
			2	0.0171915	544.409	456.563	20.690	1.0300

4.2.3 Kinetic deconvolutions in 85-DHS samples

Kinetic deconvolutions in 85-DHS samples are presented in Figure 8 for Gaussian transfer functions; and in Figure 9 for Weibull transfer functions. The difference in microstructural condition between this sample and the previous one is the presence in the latter of a larger number of defects due to a higher degree of deformation. In Figure 8, one out of the three reactions, the middle one in particular, prevails over the other two, whereas in Figure 9, with the Weibull transfer function, a first dominant reaction is observed interacting with a less prevailing one but whose enthalpy is larger than that of a second reaction obtained for samples cold-rolled to a lesser reduction.

Table 4 displays deconvolution parameters for 85-DHS samples, which are coherent with the aforesaid statement regarding Stotal and diffusive mechanisms. There seems to be a setback, however, as total areas are compared with those of 50-DHS, perhaps a product of the rearrangement of dislocations occurring when a sample is severely deformed, although in the case of Weibull transfer functions, the area of the second reaction shows a gain in enthalpy relative to the first reaction, an expected behavior owing to the larger number of rolling defects in these samples.

4.3 Kinetic parameters

The following tables, 5, 6, and 7, present the temperature of the maximum for each reaction, the transfer function used, parameters n and m, the activation energy Q, linear determination factor R2 (L), and the Arrhenius prefactor A.

The analysis of results must be carried out taking into account that the mechanisms of the resulting reactions are diffusive; that the diffusion energy of Si

in Al is 136 kJmol^{-1} in a temperature range between 480 and 620°C [58], capable of reaching 76 kJmol^{-1} between 360 to 500°C in thin foils [59]; that values between 135 and 223 kJmol^{-1} have been reported for diffusion of Fe in Al [60]; and also that for temperatures above 400°C, activation energy values from 79 to 184 kJmol^{-1} have been reported in different reactions occurring in AA8011 under different microstructural conditions [61- 63].

The fitting results in Equation (1) are presented below, provided that the value R^2 is the one to generate the best theoretical-experimental correlation.

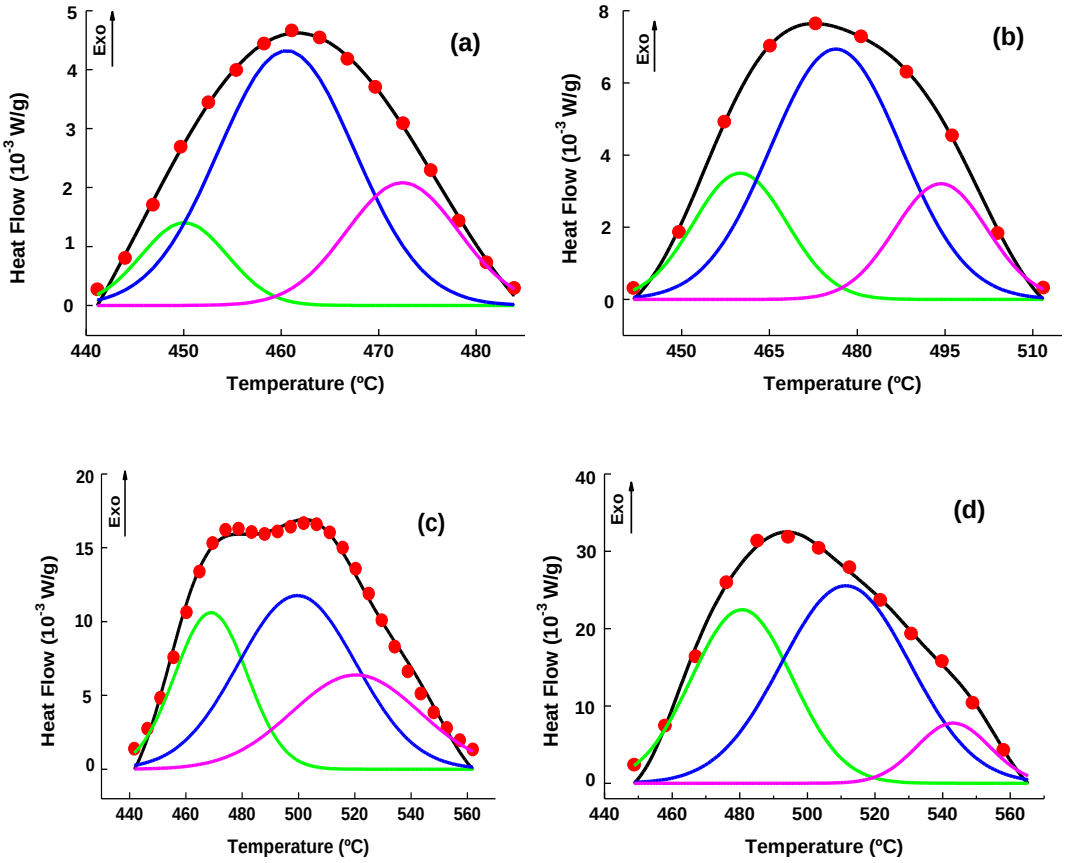

Figure 8. Deconvolution plots using Gaussian transfer function, showing the heat flow vs temperature for 85-DHS samples for different heating rates. a. 5 ºCmin^{-1} b. 10 ºCmin^{-1} c. 20 ºCmin^{-1} d. 40 ºCmin^{-1}.

Table 4. Deconvolution parameters for Gaussian and Weibull transfer functions for AA8011 85-DHS samples.

β ºC min^{-1}	S_{Total}	R^2 TF	Reaction	W_0	W_1	W_2	W_3	S
5	0.12118	0.9979 G	1	0.0014054	450.062	4.41259		0.0155
			2	0.0043246	460.560	6.98770		0.0757
			3	0.0020851	472.445	5.71864		0.0299
10	0.32796	0.9987 G	1	0.0034999	459.992	7.99367		0.0701
			2	0.0069392	476.358	11.1634		0.1942
			3	0.0032096	494.313	7.91190		0.0637
20	1.32268	0.9925 G	1	0.0106065	468.943	12.8207		0.3409
			2	0.0117635	499.563	20.9540		0.6179

			3	0.0063824	520.369	22.7499		0.3640

Table 4. Deconvolution parameters for Gaussian and Weibull transfer functions for AA8011 85-DHS samples. **Continued**.

β °C min^{-1}	S_{Total}	R^2 TF	Reaction	W_0	W_1	W_2	W_3	S
40	2.26871	0.9950 G	1	0.0224553	480.649	14.9025		0.8388
			2	0.0255473	511.330	19.0217		1.2181
			3	0.0077900	543.114	10.8462		0.2118
5	0.12118	0.9987 W	1	0.0032529	457.304	21.04796	2.30422	0.0722
			2	0.0022396	469.010	71.97259	8.89100	0.0490
10	0.32694	0.9996 W	1	0.0060734	467.700	31.65814	2.46713	0.1292
			2	0.0043673	490.298	172.4429	15.1828	0.1345
20	1.31134	0.9965 W	1	0.0160366	476.412	44.80084	2.23006	0.7765
			2	0.0113294	516.225	44.85233	2.31111	0.5348
40	2.25400	0.9987 W	1	0.0306889	491.240	54.54027	2.22808	1.8102
			2	0.0096349	536.106	625.3847	36.8966	0.4438

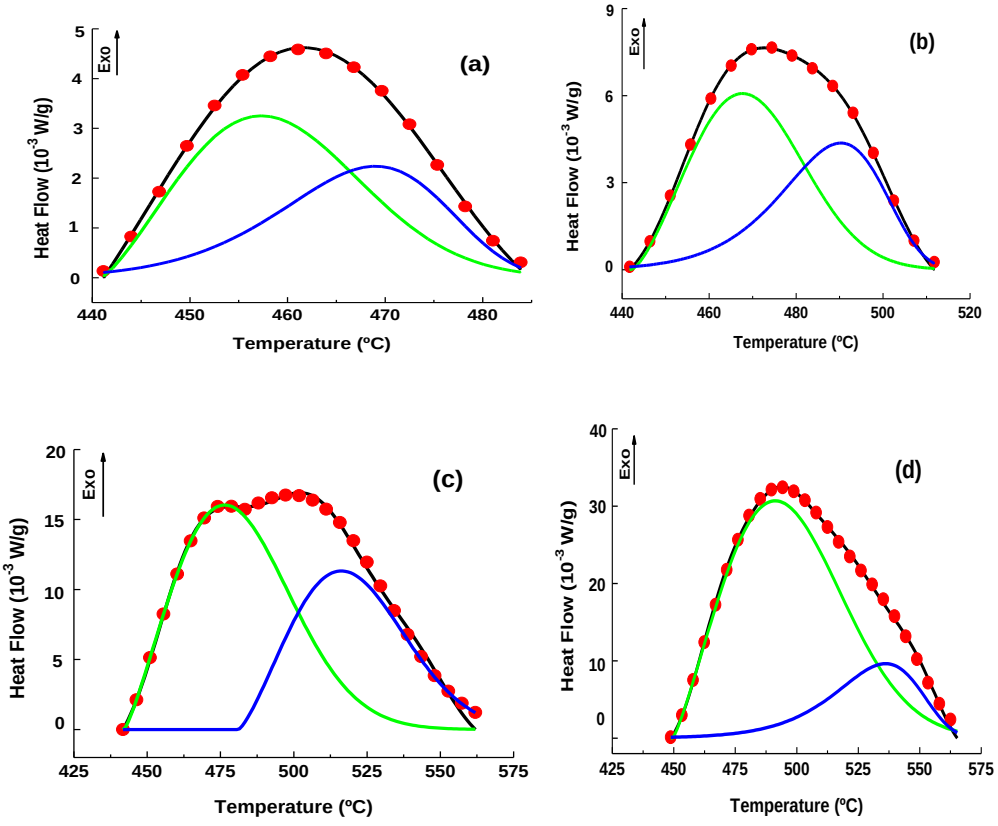

Figure 9. Deconvolution plots using Weibull transfer function, showing the heat flow vs temperature for 85-DHS Samples for different heating rates. a. 5 °Cmin^{-1} b. 10 °Cmin^{-1} c. 20 °Cmin^{-1} d. 40 °Cmin^{-1}.

4.3.1 Kinetic parameters for HS samples

Table 5 showcases the adjustment results for HS samples with both transfer functions, from which the following can be highlighted:

For Gaussian transfer functions, the first reaction holds values of n and m around 1 and 0.55, suggesting that the same kinetic function is valid for different β, akin to a sole mechanism with an activation energy reaching from 79 to 218 $kJmol^{-1}$. Values of n and m for the second reaction do not follow the same pattern as those of the first, two different types of kinetic functions being generated for β=5 and 10°C/min with activation energies over 400 kJ/mol; and for β=20 and 40°C/min with energies of 106 and 72 $kJmol^{-1}$, respectively. The third Gaussian reaction with m=0 shows a behavior associated to a reaction controlled by boundary diffusion, (Rn type with n=1.4 [43]). The activation energy values for this case are quite high, the $R^2(L)$ values being, in addition, the smallest obtained in the calculations. The asterisk indicates the existence of better $R^2(L)$ values, though their positive slopes bring forth an inconsistency with the value of Q. Reactions with high Q values are hardly harmonious with actual physical processes, an inconsistency that compromises the use of Gaussian transfer functions for the analysis of these experimental data.

For Weibull transfer functions, the first reaction shows values of $0.92<n<0.94$ and $0.47<m<0.51$, indicative of a sole kinetic function with an activation energy between 35 and 75 $kJmol^{-1}$, whereas a larger array of m values is obtained for the second reaction, showing that the data obtained at 5°C/min considerably pulls away from the single function presented by other β values. The activation energy for this reaction fluctuates between 36 and 109 $kJmol^{-1}$, these values being extremely low taking into account that this reaction occurs by Fe or Si diffusion.

4.3.2 Kinetic parameters for 50-DHS samples of an AA8011 alloy

Table 6 displays the results for 50-DHS samples for both transfer functions. The first reaction with the Gaussian transfer function shows similar n and m values for each β, and a decreasing activation energy with β located between 110 and 75 kJmol-1. The second reaction equally presents a decreasing energy except for β=40°C/min, where n and m differ from those obtained for smaller β values. The third reaction presents equal n and m values within an elevated range and activation energy. Again, the asterisk in R2 indicates a possible adjustment with other kinetic parameters but with negative values of Q.

The Weibull distribution generates well behaved n and m values with a low activation energy between 30 and 56 kJ/mol for the first reaction, whereas for the second reaction a slight n and m dispersion is observed with Q values scattered around 206 kJmol-1, these Q values being higher than those obtained with HS samples.

4.3.3 Kinetic parameters for 85-DHS samples

Table 7 showcases the kinetic parameters for 85-DHS samples. The first Gaussian reaction shows n and m values suggesting a kinetic function with decreasing Q values between 407 and 115 $kJmol^{-1}$ when β is increased. The second Gaussian reaction holds similar values of n and m except for β=40°C/min, and a large Q dispersion; whereas in the third reaction, as in the two previous microstructures, the value of m remains zero, and Q values are quite high.

With Weibull, the first reaction reports energy values between 15 and 70 $kJmol^{-1}$; and the second, higher ones between 225 and 305 kJmol-1.

This first kinetic analysis using only the fitting method of theoretical parameters on experimental data reveals that:

a) The experimental kinetics are complex and separated into simple reactions by deconvolution, but no single criterion associates these simple reactions to each other for different values of β. Considering that the same physical mechanism should be represented by the same kinetic function, i.e., same values of n and m for the same mechanism, results show that different mechanism are responsible for the dispersion of Q values.

b) As for the activation energy, an implicit dependence of ΔH on β subjects its value to both the natural logarithm of the experimental data's ratio and the kinetic function fitted on those data. The literature shows, for certain materials and for processes involving crystallization [45], a decreasing variation in Q as β grows; but there is

no mention in the literature of processes involving the coexistence of multiple mechanisms, so it is impossible to obtain the activation energy of any process without considering the experimental details, the sample geometry, and the heating rate β [47].

c) This method does not guarantee that the kinetic parameters obtained for a sequence of β values correspond to the same physical mechanism, hence the dispersion of Q values.

Table 5. Kinetic parameters for HS samples of an AA8011 alloy.

T (ºC)	β ºCmin^{-1}	TF- Reaction		n	m	Q kJmol^{-1}	A	R^2(L)
436.008	5	G	1	0.945	0.595	79.2768	1.1052E+4	0.9999
445.181	10	G	1	0.945	0.615	113.233	2.0526E+6	0.9998
454.366	20	G	1	1.035	0.465	217.935	2.8275E13	0.9999
461.730	40	G	1	1.010	0.505	218.041	1.1191E13	0.9999
461.486	5	G	2	1.400	0.160	415.904	7.7168E27	0.9989
467.027	10	G	2	1.495	0.00	403.095	2.1746E26	0.9988
471.009	20	G	2	0.960	0.640	105.609	1.3329E+5	0.9991
476.483	40	G	2	0.910	0.680	72.4560	2.8206E+2	0.9997
484.419	5	G	3	1.400	0.00	469.113	3.7439E30	0.9975*
489.894	10	G	3	1.320	0.00	593.009	∞	0.9963*
494.361	20	G	3	1.420	0.00	473.335	6.8385E29	0.9980*
504.685	40	G	3	1.390	0.0	464.831	3.2496E28	0.9976*
437.141	5	W	1	0.920	0.465	35.3244	4.26894E0	0.9998
451.022	10	W	1	0.920	0.510	61.3737	1.9220E+2	0.9998
460.422	20	W	1	0.940	0.480	63.3537	1.1773E+2	0.9997
468.758	40	W	1	0.935	0.495	74.6479	3.5959E+2	0.9998
468.323	5	W	2	0.845	0.275	109.180	3.6507E+5	0.9998
480.933	10	W	2	0.740	0.700	36.2915	2.47504E0	0.9996
489.789	20	W	2	0.775	0.670	52.7781	1.3313E+1	0.9998
503.422	40	W	2	0.805	0.605	98.9312	7.4988E+3	0.9999

Table 6. Kinetic parameters for 50-DHS samples of an AA8011 alloy.

T (ºC)	β ºCmin^{-1}	TF- Reaction		n	m	Q kJmol^{-1}	A	R^2(L)
448.700	5	G	1	0.985	0.540	110.266	1.6109E+6	0.9999
462.520	10	G	1	0.955	0.590	109.140	5.5989E+5	0.9993
471.227	20	G	1	0.915	0.660	75.5929	9.8593E+2	0.9998
482.661	40	G	1	0.940	0.605	74.9811	2.7030E+2	0.9999
468.560	5	G	2	1.105	0.495	295.724	1.8845E19	0.9989
484.110	10	G	2	1.125	0.460	215.559	7.0397E12	0.9989
499.744	20	G	2	1.040	0.355	115.597	2.0768E+5	0.9989
521.404	40	G	2	1.475	0.00	306.818	1.8999E17	0.9989

Table 6. Kinetic parameters for 50-DHS samples of an AA8011 alloy. **Continued**.

T (ºC)	β ºCmin^{-1}	TF- Reaction	n	m	Q kJmol^{-1}	A	R^2(L)
482.370	5	G 3	1.455	0.00	606.257	∞	0.9982*
511.240	10	G 3	1.360	0.00	459.806	3.1981E28	0.9974*
531.297	20	G 3	1.435	0.00	558.783	8.6309E33	0.9979*
553.430	40	G 3	1.380	0.00	491.405	2.0958E28	0.9975*
453.450	5	W 1	0.850	0.50	34.0441	2.86693E0	0.9974
471.360	10	W 1	0.920	0.515	55.5770	4.6490E+2	0.9998
491.960	20	W 1	0.845	0.570	30.2830	2.6719E-1	0.9999
512.057	40	W 1	0.830	0.595	32.8639	1.4727E-1	0.9999
483.210	5	W 2	0.890	0.565	128.629	2.1354E+7	0.9998
505.730	10	W 2	1.130	0.00	282.513	4.5579E16	0.9980
525.020	20	W 2	0.910	0.250	211.173	1.8366E11	0.9999
544.409	40	W 2	0.920	0.135	202.513	9.3904E+9	0.9999

Table 7. Kinetic parameters for 85-DHS samples of an AA8011 alloy.

T (ºC)	β ºCmin^{-1}	TF Reaction	n	m	Q kJmol^{-1}	A	R^2(L)
450.060	5	G 1	1.025	0.490	407.448	1.4162E28	0.9999
459.990	10	G 1	0.965	0.585	166.892	1.1511E10	0.9999
468.840	20	G 1	1.000	0.515	135.669	1.5962E+7	0.9999
480.649	40	G 1	0.990	0.525	115.323	1.8977E+5	0.9999
460.560	5	G 2	0.905	0.700	109.210	2.0905E+6	0.9994
476.360	10	G 2	0.990	0.600	140.628	6.8578E+7	0.9989
499.560	20	G 2	0.875	0.705	33.8929	5.6063E-1	0.9992
511.330	40	G 2	1.470	0.00	343.829	1.1530E20	0.9988*
472.440	5	G 3	1.440	0.00	1077.99	∞	0.9978*
494.310	10	G 3	1.420	0.00	807.485	∞	0.9973*
520.370	20	G 3	1.185	0.00	268.900	1.0844E15	0.9954*
543.115	40	G 3	1.310	0.00	638.310	1.6980E38	0.9957*
457.303	5	W 1	0.840	0.525	57.3963	2.8825E+2	0.9984
467.700	10	W 1	0.905	0.525	69.5353	6.6204E+2	0.9998
476.410	20	W 1	0.930	0.485	46.9284	0.4888E0	0.9998
491.240	40	W 1	0.820	0.530	14.8788	1.0970E-2	0.9994
469.010	5	W 2	0.790	0.520	224.620	1.6024E14	0.9998
490.300	10	W 2	0.865	0.380	250.365	1.2061E15	0.9979
516.230	20	W 2	1.330	0.000	305.189	3.5790E17	0.9987
536.104	40	W 2	0.880	0.175	246.916	1.2233E13	0.9999

4.4 Activation energy evaluation

This section combines isoconversion theory tenets and experimental kinetic deconvolution results obtained via calorimetric measurements for HS, 50-DHS, and 85-DHS samples [48,65,66]. Peak temperatures for different values of β are identified from the deconvolved curves, and the activation energy Q is evaluated using the isoconversion relation (Equation (2)) [48].

Columns 1 and 2 from Tables 5, 6, and 7, for HS, 50-DHS and 85-DHS samples respectively, show the temperature of the maximum of each deconvolved reaction and its respective heating rate β. From these values, ln (β/T^2) vs 1/T was plotted, the slope (-Q/R) and intercept ln(A) being determined next. Figure 10 displays the respective Kissinger plots, and Table 8 showcases the different parameters deduced from them.

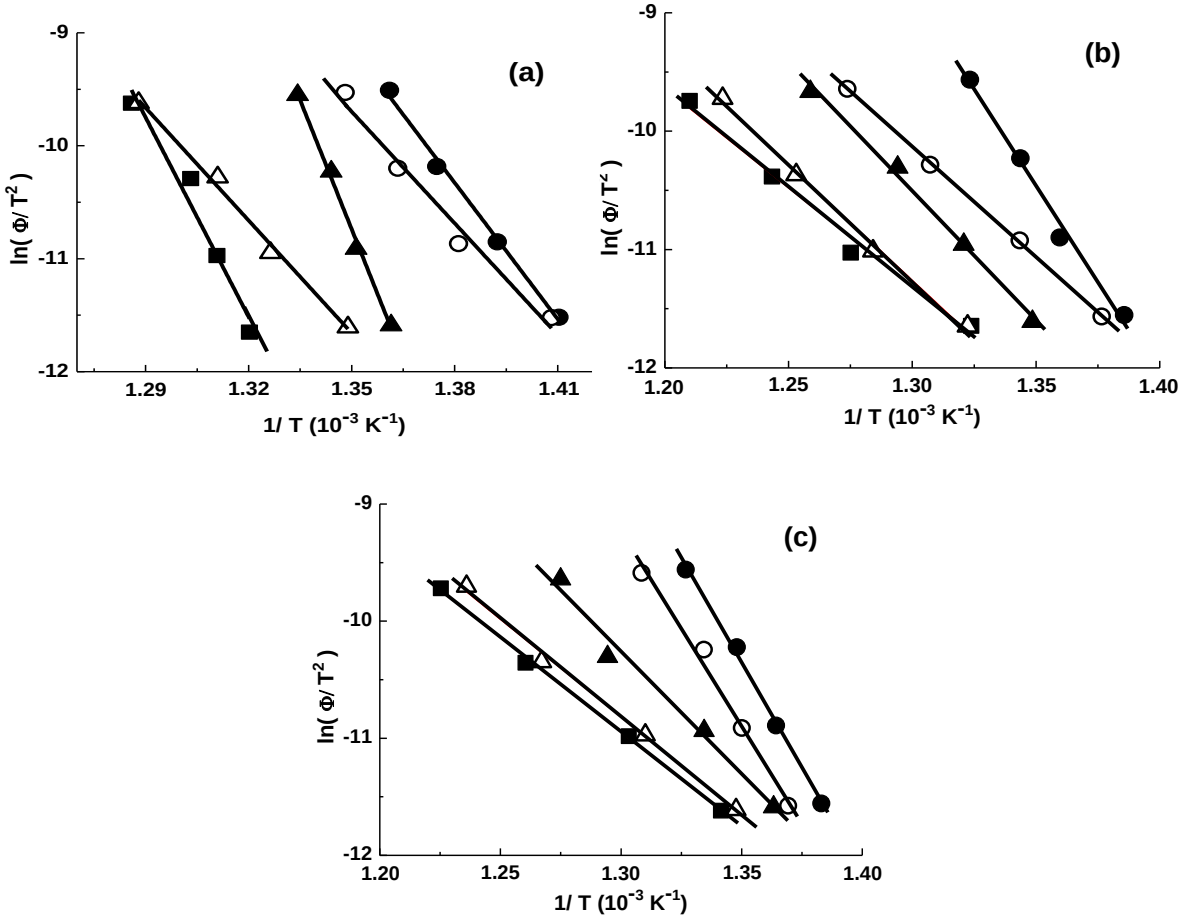

Figure 10. Kissinger plots to determine activation energy Q for different reactions deconvolved in an AA8011 alloy. a) Samples HS b) Samples 50-DHS c) Samples 85-DHS. Black symbols: Using Gaussian TF. White symbols: Using Weibull TF. Circle: First reaction. Triangle: Second reaction. Square: Third reaction.

The linearity obtained for each reaction and for every one of the microstructures studied was exceptionally good, which is reflected in values of $R^2 \geq 0.99$, except in the case of the third reaction using HS samples with Gaussian transfer functions. Comparing these energies with those obtained in the previous section via linear regression, where the same reaction with different values of β reflects important differences, makes for the conclusion that the supposed fitting uniqueness of parameters is not so; and that different sets of parameters that minimize Equation (1), for example, might be obtained. The more adjustable parameters exist, the more groups of these parameters might achieve such minimization. Based on this

reasoning, it is necessary to reduce the group of parameters minimizing Equation (1), so that the n and m dispersion can be made smaller, and thus the Q energy spectrum obtained in the previous section be in turn lessened. The energy values obtained by isoconversion are located between 139 and 489 kJmol-1, excepting the value of 633 kJmol^{-1}, reached by the second reaction in HS samples using Gaussian transfer function, which can be better explained by taking into account that these reactions are diffusive, and that the diffusion energy of the main alloying components in AA8011 are 136 kJmol^{-1} for Si in Al and up to 232 kJmol^{-1} for Fe in Al. In conclusion, isoconversion allows for more reliable energy values, and reduces the uncertainty regarding the values fitting the kinetic function; hence the need to apply an isoconversion assessment before evaluating the parameters of the latter.

Table 8. Activation energy and other parameters deduced from the linearization of Equation 8.

Samples	Reaction	TF	Slope	Ln(A)	R^2	Q (kJmol^{-1})
HS	1	G	-40.231	45.192	0.994	334.493
HS	2	G	-76.122	90.029	0.998	632.901
HS	3	G	-58.840	66.154	0.982	489.214
HS	1	W	-32.956	34.793	0.990	282.321
HS	2	W	-33.236	33.211	0.997	276.128
50-DHS	1	G	-32.407	33.286	0.995	269.442
50-DHS	2	G	-21.179	17.820	0.997	176.089
50-DHS	3	G	-16.788	10.505	0.994	139.581
50-DHS	1	W	-18.606	14.054	0.999	154.713
50-DHS	2	W	-19.480	14.066	0.997	161.963
85-DHS	1	G	-35.967	38.196	0.999	317.573
85-DHS	2	G	-20.873	16.869	0.991	173.545
85-DHS	3	G	-16.131	10.020	0.994	134.118
85-DHS	1	W	-33.131	33834	0.994	275.461
85-DHS	2	W	-16.708	10.899	0.998	138.915

4.5 Kinetic parameters deduced from isoconversion and SB combined methods

The activation energy having been evaluated through isoconversion, Qiso, there followed the evaluation of the kinetic function, applying the same methodology as in the previous section, but in this case, seeking the values of n and m linearizing Eq. (7) for a value of activation energy equal to the energy obtained by isoconversion. A well-behaved kinetic function for n and m is that which generates the highest R^2(L) value for a Q value no more than 0.5% apart from Qiso.

The parameters obtained through linear regression for homogenized samples (HS) are shown in Table 9. It shows activation energy values obtained by isoconversion (Q_{iso}) and those obtained by adjustment (Q_{SB}), as well as n and m values of the A Šesták-Berggren kinetic function and the R^2 correlation factor quotient for each transfer function used.

Q values obtained using Gaussian transfer functions are higher than those obtained using Weibull. Undoubtedly, Q values obtained for reactions 1 and 2 with Weibull may be interpreted as having been mainly generated, in lesser proportion, by Fe and Si diffusion, where undoubtedly Fe and Si rich phases coexist, possibly those of α-AlFeSi and Al3Fe, in agreement with reports by Shoji [29]. A graceful way to circumvent elaboration regarding the high values obtained when the Gaussian transfer function is used, is accepting that it is inadequate for the kinetics study of these particular experimental data. Even A values are much too high for the third reaction.

Table 10 shows the results for 50-DHS samples. In this case, Q values displayed seem valid for both

Gaussian and Weibull transfer functions. It must be taken into account that these samples are cold-rolled down to 50%; that the recrystallization process at this temperature has been completed or is in the process of being completed; and that an extra mechanism, associated to recrystallized grain growth, must be under way. The energy of the first two reactions using Gaussian transfer functions indicates that a process is indeed ongoing, whereby Fe diffusion is predominant, and Si diffusion markedly less so; whereas the third reaction might well correspond to the high-angle boundary migration that characterizes crystallized grain growth. Using Weibull transfer functions results in Q values much lower than those reported for homogenized samples, though bearing more resemblance to those of reactions 2 and 3 obtained with Gaussian transfer functions.

Table 9. Kinetic parameters deduced from combined Isoconversion-Šesták-Berggren models, for HS samples.

$Q=Q_{SB}$ kJmol^{-1}	β (ºC/min)	TF	Reaction	n	m	$Q=Q_{ISO}$ kJmol^{-1}	A	R^2(L)
333.773	5	G	1	1.435	0.065	334.493	5.9271E22	0.9991
333.451	10	G	1	1.230	0.320		2.1085E22	0.9993
334.999	20	G	1	1.170	0.335		7.1945E21	0.9997
334.277	40	G	1	1.130	0.390		2.0529E21	0.9997
630.376	5	G	2	1.870	0.000	632.901	∞	0.9952
630.601	10	G	2	2.310	0.000		∞	0.9842
631.487	20	G	2	1.865	0.000		∞	0.9951
630.834	40	G	2	1.865	0.000		∞	0.9951
487.187	5	G	3	1.455	0.00	489.214	6.9966E31	0.9973
490.358	10	G	3	1.210	0.130		3.8453E31	0.9959
486.835	20	G	3	1.460	0.00		5.9149E30	0.9978
488.452	40	G	3	1.460	0.0		1.3500E30	0.9973
281.417	5	W	1	1.655	0.000	282.321	4.9628E18	0.9978
282.314	10	W	1	1.375	0.145		1.5466E18	0.9984
281.851	20	W	1	1.390	0.165		4.0843E18	0.9982
282.174	40	W	1	1.305	0.205		1.4089E17	0.9986
274.999	5	W	2	1.680	0.000	276.128	4.0348E17	0.9746
275.239	10	W	2	1.095	0.220		8.6970E16	0.9986
275.098	20	W	2	1.135	0.125		2.1441E16	0.9989
275.220	40	W	2	1.050	0.150		5.2519E13	0.9995

Table 11 displays kinetic parameters for 85-DHS, where the behavior obtained in moderately deformed samples is emphasized. The activation energy shows two reactions, the first for each transfer function might well be associated to an Fe-rich phase precipitation, whether Fe_3Al or β-AlFeSi; whereas the third Gaussian reaction and the second Weibull reaction coincide in energy value, in agreement with the high-angle boundary diffusion referenced in [2,51,67]. The Q value for the second reaction using Gaussian transfer function coincides with that obtained for 50-DHS samples.

This second kinetic analysis reveals n and m dispersion values lower than those obtained using the previous method. This dispersion is attributable to the dependence of the activation energy Q on α, and to the fact that the Kissinger method used can only be considered as an isoconversion method for

fully symmetric kinetic reactions where the Tp value corresponds to a conversion around α = 0.5, this being valid when Gauss transfer functions are used, but not when using Weibull functions.

Table 10. Kinetic parameters deduced from combined Isoconversion-Šesták-Berggren models, for 50-DHS samples.

$Q=Q_{SB}$ kJmol^{-1}	β^{o} Cmin^{-1}	FT Reaction	n	m	$Q=Q_{ISO}$ kJmol^{-1}	A	R^2
268.296	5	G 1	1.260	0.250	269.442	4.3248E17	0.9994
268.739	10	G 1	1.185	0.345		1.1879E17	0.9994
269.463	20	G 1	1.200	0.355		3.9162E16	0.9992
269.206	40	G 1	1.305	0.200		6.9225E15	0.9993
176.707	5	G 2	0.990	0.625	176.089	8.0954E10	0.9989
176.619	10	G 2	1.070	0.525		1.4603E10	0.9989
175.305	20	G 2	1.160	0.395		2.2246E09	0.9989
176.198	40	G 2	1.190	0.345		5.1125E08	0.9988
140.093	5	G 3	0.935	0.615	139.581	1.0787E08	0.9967
139.137	10	G 3	0.925	0.545		1.5004E07	0.9940
138.884	20	G 3	0.925	0.595		4.8655E06	0.9951
139.494	40	G 3	0.920	0.560		1.2703E06	0.9941
155.471	5	W 1	1.175	0.235	154.713	1.4679E09	0.9972
154.441	10	W 1	1.150	0.315		3.9031E08	0.9989
154.724	20	W 1	1.175	0.245		7.9783E07	0.9983
154.250	40	W 1	1.170	0.190		1.6677E07	0.9986
161.421	5	W 2	0.920	0.535	161.963	3.9153E09	0.9997
162.316	10	W 2	0.925	0.340		4.0651E08	0.9984
162.042	20	W 2	0.850	0.415		1.1435E08	0.9995
162.063	40	W 2	0.865	0.300		2.5104E07	0.9999

Table 11. Kinetic parameters inferred from combined Isoconversion-Šesták-Berggren models for 85-DHS samples.

$Q=Q_{SB}$ kJmol^{-1}	β °Cmin^{-1}	TF Reaction	n	m	$Q=Q_{ISO}$ kJmol^{-1}	A	R^2
319.118	5	G 1	0.975	0.540	317.573	5.9073E20	0.9998
317.853	10	G 1	1.115	0.430		6.5345E20	0.9996
317.201	20	G 1	1.280	0.225		9.4382E19	0.9994
316.827	40	G 1	1.340	0.160		1.7131E19	0.9993
173.645	5	G 2	0.960	0.640	173.545	8.0643E10	0.9993
173.147	10	G 2	1.030	0.550		1.2565E10	0.9989
172.878	20	G 2	1.185	0.340		1.3433E09	0.9989
173.837	40	G 2	1.140	0.400		5.7934E08	0.9987

Table 11. Kinetic parameters inferred from combined Isoconversion-Šesták-Berggren models for 85-DHS samples. **Continued**.

Q=QSB kJmol^{-1}	β ºCmin^{-1}	TF Reaction	n	m	Q=Q$_{ISO}$ kJmol^{-1}	A	R^2
134.492	5	G 3	0.815	0.695	134.118	1.0896E08	0.9848
134.756	10	G 3	0.865	0.670		2.2302E07	0.9873
134.434	20	G 3	0.915	0375		1.5953E07	0.9918
134.165	40	G 3	0.825	0.610		9.7962E05	0.9817
274.243	5	W 1	1.110	0.310	275.461	8.9681E17	0.9977
274.380	10	W 1	1.255	0.240		1.7907E17	0.9985
274.705	20	W 1	1.525	0.020		3.3228E16	0.9982
274.296	40	W 1	1.670	0.000		6.0538E15	0.9960
139.006	5	W 2	0.725	0.645	138.915	1.5129E08	0.9993
139.565	10	W 2	0.765	0.625		3.2357E07	0.9996
138.948	20	W 2	0.980	0.300		3.7609E06	0.9921
139.364	40	W 2	0.765	0.525		1.4631E06	0.9999

5. CONCLUSIONS

An above-400ºC study of an Al-Fe-Si alloy (AA8011) was carried out by calorimetric curve deconvolution obtained by DSC using different transfer functions and by combining Šesták-Berggren and isoconversion methods, with the following conclusions:

1. A kinetic analysis based solely on the adjustment of parameters associated to the kinetic function does not guarantee the absolute minimum demanded by linear regression, so that different relative minima that meet the condition of linearity may be obtained. The isoconversion method, by directly supplying the activation energy, reduces this problem to obtaining the kinetic function that replicates that energy value.
2. The deconvolution of experimental DSC plots by employing Gaussian and Weibull functions evinces the coexistence of different overlapping reactions happening along the main processes and affecting their kinetic parameters. It took three reactions to reproduce the experimental kinetic when using Gaussian transfer function, whereas only two were needed when Weibull functions were used. This is possible since the asymmetry associated to Weibull better covers the start and endpoints of the experimental kinetic.
3. In the case of homogenized samples, the Gaussian transfer function results in physically inadequate outcomes, whereas the Weibull transfer function predicts the coexistence of two Fe-rich phases, the first of which corresponds, according to the literature, to AlFeSi; and the second, probably, to Al_3Fe [29,30].
4. For highly deformed samples, Gaussian transfer functions predict two reactions whose activation energy is in agreement with Fe diffusion energy; whereas the third reaction reflects activation energy in conformity with the energy associated to the diffusion process of high-angle grain boundaries. Weibull transfer functions yield an Fe-rich phase and a second reaction associated to the diffusion process of grain boundaries located around 136 kJmol^{-1}, similar value for both transfer functions.
5. It follows that in multicomponent alloys, DSC measurements generate a heat flow which in turn encompasses several reactions; and the particular information borne by each of them can be inferred by using deconvolution methods.

6. The combination of isoconversion and linear regression are presented as the adequate methodology to determine the kinetic triplet.

6. ACKNOWLEDGEMENT

This work is supported by the Office of Academic Planning at the Universidad de Oriente through POA Project PN 5.5/2010. We acknowledge our thanks to Carlos Mota for the translation of this manuscript.

7. REFERENCES

[1]. Gokhale AM, Iswaran CV, DeHoff RT. Use of the stereological counting measurements in testing theories of growth rates. Metall. Trans. A .1979; 10A (9): 1239-1245.

[2]. Doherty RD, Hughes DA, Humphreys FJ, Jonas JJ, Jenson DJ, Kassner ME, King WE, McNelley TR, McQueen HJ, Rollett AD. Current issues in recrystallization: a review. Mat. Sci. Eng. A 1997; 238: 219-274.

[3]. Haessner F (editor). Systematic survey and basic problems of recrystal¬lization. Recrystallization of metallic materials. Stuttgart: Dr. Riederer Verlag. 1978; 1-10.

[4]. Rangel Rios P, Siciliano F Jr, Zschommler Sandim HR, Lesley Plaut R. Padilha AF. Nucleation and growth during recrystallization. Materials Research. 2005; 8: 225-238.

[5]. Humphreys FJ. Hatherly M. Recrystallization and Related Annealing Phenomena, 2ed. Pergamon Press Oxford, England. 2004; 285-319.

[6]. Krishna KS, Vigneshwaran S, Chandra Sekhar K, Akella Sarma SR, Sivaprasad K, Narayanasamy R, Venkateswarlu K. Mechanical behavior and void coalescence analysis of cryorolled AA8090 alloy. Int J Adv Manuf Technol.2016; DOI 10.1007/s00170-016-8863-2.

[7]. Roy RK. Recrystallization Behavior of Commercial Purity Aluminium Alloys. 2010; http://dx.doi.org/10.5772/58385

[8]. Roy RK, Kar S, Das K, Das S. Microstructures and tensile properties of commercial purity aluminium alloy AA1235 under different annealing conditions. Materials Letters. 2005; 59: 2418 – 2422.

[9]. Wang X, Guan RG, Tie D, Shang YQ, Jin HM, Li JCH. Microstructural Evolution of Al-1Fe (Weight Percent) Alloy During Accumulative Continuous Extrusion Forming. Met. Mat. Trans. B. 2018; https://doi.org/10.1007/s11663-018-1185-z

[10]. Khatami R, Fattah-alhosseini A, Mazaheri Y, Keshavarz MK, Haghshenas M. Microstructural evolution and mechanical properties of ultrafine grained AA2024 processed by accumulative roll bonding. Int J Adv Manuf Technol. 2017; DOI 10.1007/s00170-017-0547-z

[11]. Lee DN. Evolution of Recrystallization Textures in Cold-Rolled Commercially Pure Aluminum. Materials Science Forum. 2016; 879: 2365-2370.

[12]. Miszczyk MM, Paul H, Driver JH, Poplewska J. The influence of deformation texture on nucleation and growth of cube grains during primary recrystallization of AA1050 alloy. Acta Materialia. 2017; 129: 378-387.

[13]. Torres T, Bisbal R, Camero S, Llanos C. Estudio del efecto del tratamiento térmico de homogeneización en la microestructura y propiedades mecánicas de una aleación de aluminio AA8011. Acta Microscópica. 2011; 20 (2):165-173.

[14]. Aghaie-Khafri M. Formability of AA8011 aluminum alloy sheet in homogenized and unhomogenized conditions. J. Mat. Sci. 2004; 39: 6467 – 6472.

[15]. Subramani K, Alagarsamy SK, Chinnaiyan P, Chinnaiyan SN. Studies on testing and modelling of formability in aluminium alloy sheet forming. Trans. of Famena XLII-2. https://doi.org/10.21278/TOF.42206. 2018; 67-82.

[16]. Dugár Z, Barkóczy P, Béres G, Kis D, Bata A, Dugár T, Weltsch Z. Determination of Recrystallization Temperature of Varying Degrees Formed Aluminium, by DMTA Technique. International J. Mech and Mechatronics Eng. 2015: 9(3): 253-256.

[17]. Lauridsen EM. The 3D X-ray diffraction microscope and its application to the study of recrystallization kinetics. 2001; Denmark. Forskningscenter.Risoe. Risoe-R; No. 1266 (EN).

[18]. Kuhbach M, Bruggemann T, Molodov KD,Gottstein G. On a Fast and Accurate In Situ Measuring Strategy for Recrystallization Kinetics and Its Application to an Al-Fe-Si Alloy. Met. Mat. Trans. A.2015; 46A:1337-1348.

[19]. Adam K, Zöllner D, Field DP.3D Microstructural Evolution of Primary Recrystallization and Grain Growth in Cold Rolled Single-Phase Aluminum Alloys. 2017; Modelling Simul. Mater. Sci. Eng. in press https://doi.org/10.1088/1361-651X/aaa146

[20]. Shabaniverki S, Serajzadeh S. The kinetics of isothermal and non-isothermal recovery within cold-rolled aluminum alloy. Multidiscipline

Modeling in Materials and Structures. 2015; 11 (1):88-101,

[21]. Sepehrband P, Wang X, Jin H, Esmaeili S. Interactive microstructural phenomena during non-isothermal annealing of an Al-Mg-Si-Cu alloy. Materials Characterization. 2018;https://doi.org/10.1016/j.matchar.2018.01.014.

[22]. Moghanaki SK, Kazeminezhad M. Effects of non-isothermal annealing on microstructure and mechanical properties of severely deformed 2024 aluminum alloy. Trans. Nonferrous Met. Soc. China.2017; 27: 1−9.

[23]. Luiggi NJ, Valera M, Prin J. Linares M. Estudio de la aleación AA8011 laminada usando DSC y MET. Acta Microscópica. 2013; 22(1): 105-110.

[24]. Luiggi NJ, Valera M, Rodríguez JP, Prin J. Experimental Study of the Interaction between Recrystallization and Precipitation Processes of an AA8011 Commercial Alloy. J. Metallurgy ID 345945. 2014; 17 pages.

[25]. Luiggi NJ. Kinetic Analysis of Recovery, Recrystallization, and Phase Precipitation in an Al-Fe-Si Alloy Using JMAEK and Sesták–Berggren Models. Met. Mat. Trans. B. 2015; 46(3): 1376-1399.

[26]. García–Cordovilla C, Louis E. A differential scanning calorimetry study of recrystallization and its interaction with precipitation in Al-Fe-Si commercial alloys (AA1145 and AA8011). J. Mater. Sci. 1986; 21: 971-979.

[27]. Luiggi NJ. A Preliminary Study of the Phase Transformations in Rolled Al-Fe-Si Alloy, Met. Mat. Trans. A . 2010; 41: 3271-3275.

[28]. Roy RJ, Kar S, Das S. Evolution of microstructure and mechanical properties during annealing of cold-rolled AA8011 alloy. Journal of Alloys and Compounds. 2009; 468: 122–129

[29]. Shoji R, Fujikura C. Precipitation of Fe and Si in Cold Rolled Al-Fe-Si Sheet during Annealing. Key Eng. Materials. 1990; 44/45: 163-180.

[30]. Raghavan V. Al-Fe-Si (aluminum-iron-silicon). Journal of Phase Equilibria. Kinetic characterization of post recrystallization. 2002; 23 (4): 362-366.

[31]. Vybornov M, Rogl P, Sommer F. On the thermodynamic stability and solid solution behavior of the phasesτ5-Fe2Al7.4Si and τ6-Fe2Al9Si2. J. Alloys Compd. 1997; 247 (1/2): 154-157.

[32]. Stefaniay V, Griger A, Turmezey T. Intermetallic phases in the aluminium-side corner of the AlFeSi-alloy system. J. Mater. Sci. 1987; 22: 539-546.

[33]. Sun CY, Mondolfo LF. A Clarification of the Phases Occuring in Al-Rich Al-Fe-Si Alloys. J. Inst. Met. 1967; 95: 384-395.

[34]. Khalifa W, Samuel FH, Gruzleski JE. Iron intermetallic phases in the Al corner of the Al-Si-Fe system. Met. Mat. Trans. A. 2003; 34A: 807-825.

[35]. Kumar R, Gupta A, Kumar A, Chouhan RN, Khatirkar RK. Microstructure and texture development during deformation and recrystallization in strip cast AA8011 aluminum alloy. Journal of Alloys and Compounds. (2018), doi: 10.1016/j.jallcom.2018.01.280.

[36]. Rafaja D. Deconvolution versus convolution – a comparison for materials with concentration gradient, Materials Structure. 2000; 7 (2): 43-50.

[37]. Rey A, Casas I, Giménez J, Quiñones J, de Pablo J. Effect of temperature on studtite stability: Thermogravimetry and differential scanning calorimetry investigations. J. Nucl. Mat.2009; 385: 467-473.

[38]. Kitisy G, Gomez-Rosz JM, Tuyn JWN (1998) Thermoluminescence glow-curve deconvolution functions for first, second and general orders of kinetics. J. Phys. D: Appl. Phys. 1998; 31: 2636-2641.

[39]. Luiggi NJ and Betancourt A (1994) Multiphase precipitation of carbides in Fe-C systems: Part I. Model based upon simple kinetic reactions. Met. Mat. Trans. B. 1994; 25B: 917-925.

[40]. Luiggi NJ and Betancourt A. Multiphase precipitation of Carbides in Fe-C system. II. Model based upon Complex kinetic reactions. Met. Mat. Trans. B. 1994; 25B: 927-935.

[41]. Perejón A., Sánchez-Jiménez PE, Criado JM, Pérez-Maqueda. LA Kinetic analysis of complex solid-state reactions. A new deconvolution procedure. J. Phys. Chem. B. 2011; 115:1780-1791.

[42]. Luiggi NJ and Valera M. Kinetic study of phase precipitation of an aa7075 alloy under T6 and T7 temper. Rev. LatinAm. Metal. Mat. 2017; 37 (2): 160-178.

[43]. Luiggi NJ. Aquilanti–Mundim deformed Arrhenius model in solid-state reactions. Theoretical evaluation using DSC experimental data. J Therm Anal Calorim. 2016; 126(3):1175-1184.

[44]. Sesták J, Berggren G. Study of the kinetics of the mechanism of solid-state reactions at increasing temperature, Thermochim Acta. 1971; 3: 1-12.

[45]. Šesták J. Science of Heat and Thermophysical Studies: a generalized approach to thermal

analysis. Elsevier, Amsterdam . 2005.

[46]. Yunjung Ch, Minsu J, Young-Kook L. Effect of Heating Rate on the Activation Energy for Crystallization of Amorphous Ge2Sb2Te5 Thin Film. Electrochemical and Solid-State Letters. 2009; 12(7): F17-F19

[47]. Toft Sørensen O, Rouquerol J (Eds). Sample Controlled Thermal Analysis: Origin, Goals, Multiple Forms Applications and Future. Springer 71. 2003.

[48]. Luiggi NJ. Comments on the Analysis of Experimental Data in Nonisothermal Kinetics. Metall. Mater. Trans A. 2003; 34A: 2679-82.

[49]. Šesták J, Maleck J. Diagnostic limits of phenomenological models of heterogeneous reactions and thermal analysis kinetics Solid State Ionics. 1993; 63-65: 245-254.

[50]. Henderson DW. Experimental analysis of non-isothermal transformations involving nucleation and growth. J. Therm. Anal. 1979;15: 325-331.

[51]. Huang Y, Humphreys FJ. Subgrain growth and low angle boundary mobility in aluminium crystals of orientation {110}<001>. Acta Mater. 2000; 48: 2017-2030.

[52]. Svoboda R, Málek J. Extended study of crystallization kinetics for Se–Te glasses, J. Therm. Anal. Cal. 2013; 111: 161-171.

[53]. Oppenheim AV, Schafer R. Discrete-Time Signal Processing. Prentice Hall do Brasil, Ltda. Rio de Janeiro. 1989.

[54]. Mendel J, Burrus CS. Maximum-Likelihood Deconvolution: A Journey into Model-Based Signal Processing. Springer-Verlag, New York.1990.

[55]. Guo H. A simple algorithm for fitting a Gaussian function. IEEE Sign. Proc. Mag. 2011; 28(9) 134-137.

[56]. Abernethy RB. The New Weibull Handbook, 3rd Edn. Distributed by Gulf Pub. Co. 1999.

[57]. Langsrud Y. Silicon in commercial aluminium alloys-what becomes of its during DC casting. Key Eng. Mat. 1990; 44-45: 95-116.

[58]. Fujikawa SI, Hirano KI, Fukushima Y. Diffusion of silicon in aluminum. Met. Trans A. 1978; 9A: 1811-1815.

[59]. McCaldin JO, Sankur H (1971) Diffusivity and solubility of Si in the Al metallization of integrated circuits. Appl.Phys. Lett. 1971; 19: 524-527.

[60]. Mantl S, Petry W, Schroeder K, Vogl G. Diffusion of iron in aluminum studied by Mössbauer spectroscopy. Phys. Rev. B. 1983; 27:5313-5331.

[61]. Luiggi NJ. Characterization by thermoelectric power of a commercial aluminum-iron-silicon alloy (8011) during isothermal precipitation, Met. Mat. Trans. A. 1998; 29A: 2669-2677.

[62]. Puchi ES, Fajardo B, Valera JV. Recrystallization of commercial twin-Roll Cast Aluminum-iron-silicon Alloy Homogenized at 853 K. Proc. 4th Int. Conf. On Aluminium alloy. T.H. Sanders and E.A. Starke jrs. Eds., Atlanta, GA. 1994; 1:18-25

[63]. Lendvai J, Honyek H, Juhász A, Kovacs I. A differential scanning calorimetry study of the release of stored energy in an Al-Fe alloy, Script. Metall.1985; 19(8) 943-946.

[64]. Choi Y, Jung M, Lee YK. Effect of Heating Rate on the Activation Energy for Crystallization of Amorphous Ge2Sb2Te5 Thin Film. Electrochem Sol State Letters. 2009; 12(7): F17-F19.

[65]. Vyazovkin S and Wight CA. Model-free and model-fitting approaches to kinetic analysis of isothermal and nonisothermal data. Thermochim. Acta. 1999; 340/341: 53-68.

[66]. Vyazovkin S, Burnham AK, Criado JM, Pérez-Maqueda LA., Popescu C, Sbirrazzuoli N. ICTAC Kinetics Committee recommendations for performing kinetic computations on thermal analysis data. Thermochim. Acta. 2011; 520: 1-19.

[67]. Huang Y and Humphreys FJ. Measurements of grain boundary mobility during recrystallization of a single-phase aluminium alloy, Acta Mater. 1999; 47: 2259-2268.C.C. Silva, A.G. Thomazine, A.G. Pinheiro, J.F.R. Lanciotti, J.M. Sasaki, J.C. Goes, A.S.B. Sombra, Journal of Physics and Chemistry of Solids **63** (2002) 1745-1757.

8. APENDIX

Derivation of equation (1)

The reaction rate taken from the theory of chemical reactions for isothermal processes is given by

$$\frac{d\alpha}{dt} = K(T)F(\alpha) \qquad \text{(A1)}$$

Considering the heating ratio β = dT/dt, this same expression can be used for non-isothermal processes,

$$\beta\frac{d\alpha}{dT} = K(T)F(\alpha) \qquad \text{(A2)}$$

Experimentally, the extension of the conversion or transformed fraction α, associated with the reaction, can be deduced from the heat flow curve as a function of time considering that in the isothermal case α is defined, by:

$$\alpha = \frac{\int_0^{t\alpha} \Delta H dt}{\int_0^{tf} \Delta H dt} \quad \text{(A3)}$$

And in the non-isothermal case

$$\alpha = \frac{\int_0^{T\alpha} \Delta H dT}{\int_0^{Tf} \Delta H dT} \quad \text{(A4)}$$

where t_α (T_α) represents the time (Temperature) elapsed for the reaction to reach a transformed fraction α and t_f (T_f) the time (Temperature) for the reaction to occur completely. The integral of the denominator represents the total area under the curve and we designate it with the letter S. Deriving α in A3 with respect to time (A4 with respect to Temperature) we obtain the relation

$$\frac{d\alpha}{dt} = \frac{\Delta H_\alpha}{S} \quad \text{(A5)}$$

$$\frac{d\alpha}{dT} = \frac{\Delta H_\alpha}{S'} \quad \text{(A6)}$$

Note that in A6 the area is written as S' to differentiate the gauging unity from that at A5. Combining A1 and A5 in the isothermal case, and A2 with A6 for the non-isothermal case, we obtain:

$$\frac{d\alpha}{dt} = K(T)F(\alpha) = \frac{\Delta H_\alpha}{S} \quad \text{(A7)}$$

$$\frac{d\alpha}{dT} = \frac{K(T)F(\alpha)}{\beta} = \frac{\Delta H_\alpha}{S'} \quad \text{(A8)}$$

considering that the reaction constant follows an Arrhenius relationship, K (T) is defined as

$$K(T) = Aexp\left(-\frac{Q}{RT}\right) \quad \text{(A9)}$$

And that the kinetic function F (α) in the two-parameter model of Šesták -Berggren is defined by:

$$F(\alpha) = (1-\alpha)^n \alpha^m \quad \text{(A10)}$$

For the isothermal case, the expressions A9 and A10 are substituted in A7 and the neperian logarithm is taken, generating Equation (1)

$$\ln\left(\frac{\Delta H_\alpha}{S(1-\alpha)^n \alpha^m}\right) = \ln(A) - \frac{Q}{RT} \quad \text{(1)}$$

While that expression, following the same procedure, in the non-isothermal case, is written as

$$\ln\left(\frac{\beta \Delta H_\alpha}{S'(1-\alpha)^n \alpha^m}\right) = \ln(A) - \frac{Q}{RT} \quad \text{(A11)}$$

Note that both (1) and (A11) have similar functional forms when we incorporate in A11 the term ln (β) into the term ln (A) and define A '= A / β.

9. SYMBOL LIST

ΔH: Heat flow
S: Area under the heat flow curve
α: Fraction transformed, conversion extension
F (α): Kinetic function
K (T): Reaction constant
n, m: Coefficients of Šesták -Berggren
A: Arrhenius prefactor
Q: Apparent activation energy
Q_{SB}: Activation energy deduced from the Šesták-Berggren model
Q_{ISO}: Activation energy deduced from the isoconversion scheme
R: Universal gas constant
T: Temperature
t: Time
β: Heating rate
R^2: Determination coefficient of the regression
N: Validation coefficient of the Isoconversion
X (t): Input signal
Y (t): Output signal
g (t): General transfer function
W: Gauss or Weibull transfer function
Wi: Transfer function parameters
S_{Total}: Total area, sum of area for each deconvolved reaction
TF: Type of transfer function (G: Gauss; W: Weibull)